Journal of Inorganic and Organometallic Polymers and Materials (2024) 34:161–174
https://doi.org/10.1007/s10904-023-02807-5

RESEARCH

Investigation of Structural, Morphological and Photoluminescence Properties of Electrospun Cu@PMMA Nanofibers

Yasemin Acar[1] · Elif Gungor[1] · Mustafa Burak Coban[2] · Fatma Kuru[3] · Hulya Kara Subasat[4]

Received: 15 May 2023 / Accepted: 17 July 2023 / Published online: 5 August 2023

Abstract
In this work, a tetrameric Cu(II) Schiff base complex [Tetrakis((μ_3-N-(3,5-dichlorosalicyclideneamino)ethanolato)-Cu(II))], (**1**), has been synthesized and structurally characterized by single crystal X-ray diffraction technique. In different concentrations (5–20 wt%), complex (**1**) has been doped into poly(methylmethacrylate) (PMMA) as the polymer matrix using by electrospinning technique to form Cu@PMMA nanofibers. Both complex (**1**) and electrospun Cu@PMMA nanofibers were characterized using various techniques including field emission scanning electron microscopy (FESEM), photoluminescence (PL) and Fourier transform infrared (FT-IR) spectroscopy. The photoluminescence (PL) characteristics of Cu@PMMA composite fibers in the solid-state were studied at room temperature. Furthermore, the temperature-dependent PL properties of Cu@PMMA nanofibers, with a weight% of 15%, were investigated within a temperature range of 10–300 K. Cu@PMMA nanofibers exhibited blue emission with excitation wavelength of 349 nm. Brilliant values of the chromaticity coordinates of the prepared photoluminescent nanofibers predict their possible use in blue solid-state lighting applications.

Keywords Tetrameric Cu(II) complex · Crystal structure · Electrospinning technique · Luminescent nanofibers

1 Introduction

Nanotechnology has applications in almost every field such as physics, chemistry, biology, textile, mechanical, electrical and tissue engineering, medicine, the pharmaceutical industry, the defense industry and space research [1–5]. One of the most important goals of nanotechnology is the design and production of new materials on the nanoscale and the use of existing nanostructures or particles in new applications by making them more functional. Nanofibers as a member of the nanomaterial class have high surface-to-volume ratios and small pore sizes and show superior mechanical performance compared to many other materials [6]. For this reason, by benefiting from the developments in nanoscience and nanotechnology, it has been started to produce and investigate their superior properties new materials with increased properties in all fields such as computers that work much faster, clothes that can adapt to the body, systems that create and renew themselves, nanorobots that find and destroy diseased cells, molecular food synthesis and war equipment [7–11]. Nanofibers are used in many applications such as medical and pharmaceutical applications such as drug and gene delivery systems, wound-burn sealants, artificial blood vessels and artificial organs-tissues [12–16]. Many methods are used in the production of nanofibers such as phase separation, self-assembly, fiber drawing, melt fibrillation, template synthesis, interface polymerization, solution spinning and electrospinning [17]. Among these, electrospinning is a method used to produce nanofibers from solutions or melts and electric force is applied to perform the spinning process [18–20]. Electrospun nanofibers are used in many application areas such as sensor construction, template development for the preparation of functional nanotubes, production of non-woven yarns, conductive polymer production and filtration systems [3, 21–24].

✉ Yasemin Acar
yaseminyahsi@gmail.com

1 Department of Physics, Faculty of Science and Art, Balikesir University, Balıkesir, Turkey

2 Center of Science and Technology Application and Research, Balikesir University, Balıkesir, Turkey

3 Department of Chemistry, Molecular Nano-Materials Laboratory, Graduate School of Natural and Applied Sciences, Mugla Sitki Kocman University, Mugla, Turkey

4 Department of Energy, Molecular Nano-Materials Laboratory, Graduate School of Natural and Applied Sciences, Mugla Sitki Kocman University, Mugla, Turkey

The tetrameric Cu(II) transition metal complex constitutes an important class of compounds in cubic structures in the form of M_4L_4 of four metal ions linked by hydroxo, alkoxo, azido or sulfido bridges and are also promising catalytic agents [25–34]. Among such complexes, many alkoxo-bridged cubic complexes have become an important subject of study as they also exhibit interesting structural, magnetic and biological properties. In particular, polynuclear Cu(II) complexes are noteworthy for their involvement in many metabolic processes in living organisms and have become important model compounds in the investigation of the physical and chemical behavior of biological copper systems [35].

In recent years, various polymers such as polymethyl methacrylate (PMMA), polyvinyl alcohol (PVA), polystyrene (PS), polyacrylonitrile (PAN), polyvinyl pyrrolidone (PVP) and polyethylene oxide (PEO) have been used with different functional additives for fabricating the light-emitting nanofibers [36–39]. PMMA which is one of the most adaptable polymers for many fields has a wide range of potential applications such as engineering, optical, biomedical, polymer conductivity, sensors, food packaging and nanotechnology [40]. PMMA can be modified with nano and molecular structures to obtain a wide variety of functional materials. In this study, PMMA has been chosen as a polymer and a tetrameric Cu(II) complex has been used to obtain electrospun Cu@PMMA nanofibers. Limited research has been conducted to investigate the morphological, mechanical and photoluminescent characteristics of electrospun nanofibers incorporating various copper complexes, as indicated in Table S1 (in Supp. Info.) [41–46]. It is understood from this table that the researches on organic and/or inorganic component doped electrospun nanofibers will shed light on future studies on new functional nanofibers and their useful applications. To the best of our knowledge, there have been no previous studies focusing on the analysis of the structural, morphological, and photoluminescent properties of Cu@PMMA nanofibers doped with Cu(II) complex using the electrospinning technique. Hence, this article makes a significant contribution to the existing literature by presenting the preparation of Cu@PMMA composite nanofibers through the utilization of the electrospinning technique, incorporating complex (**1**) at varying concentrations (5–20 wt%). Furthermore, it focuses on the examination of the solid-state photoluminescence properties of these nanofibers at room temperature using UV laser excitation at 349 nm in the visible region. Temperature dependent PL properties of Cu@PMMA nanofibers (15 wt%) was also investigated in the temperature range 10–300 K. The composite nanofibers exhibited blue emission with 349 nm excitation wavelength. From the bright values of the CIE chromaticity coordinates of the obtained photoluminescent nanofibers, it is estimated that their use in blue solid-state lighting applications is possible.

2 Experimental

2.1 Materials and Physical Measurements

In the synthesis procedure, copper(II) chloride ($CuCl_2$) of 99.99% purity, 3,5-dichlorosalicylaldehyde (99%), ethanolamine (99%), methanol (99.8%), N,N-dimethylformamide (DMF; 99.8%) and PMMA were purchased from Merck KGaA, Darmstadt, Germany and used without any purification. The molecular weight of PMMA selected for the preparation of nanofibers in this study is 350,000 by GPC. The elemental analyses (C, H, N) were realized by standard methods. Infrared spectra were measured in the range of 4000–600 cm^{-1} with a Perkin-Elmer 1600 Spectrum. The photoluminescence spectra in the solid state and the visible region were measured with an ANDOR SR500i-BL Photoluminescence Spectrometer at ambient temperature. The measurements were performed by the use of an excitation source (349 nm) of a Spectra-physics Nd:YLF laser with a 5 ns pulse width and 1.3 mJ of energy per pulse.

2.2 Synthesis of Complex (1)

To a methanol solution (30 mL) of 3,5-dichlorosalicylaldehyde (1 mmol) was added a methanol solution (20 mL) of ethanolamine (1 mmol) with stirring at room temperature for 1 h. To the resulting yellow solution was added $CuCl_2$ (1 mmol) in 50 mL methanol and stirred in air condition at room temperature for 1 h more. After the resulting clear green solution was kept at room temperature for 3 weeks, the single crystals of complex (**1**) suitable for X-ray analysis were obtained. The synthetic route of the copper complex is outlined in Scheme 1. Complex (**1**): Green crystals, yield 78%. Anal. Calc. for complex (**1**): $C_{36}H_{28}Cl_8Cu_4N_4O_8$: Calc.: C, 36.57; H, 2.39; N, 4.74%. Found: C, 37.01; H, 2.54; N, 4.65%.

2.3 Preparation of Cu@PMMA Nanofibers by Electrospinning Technique

To prepare the electrospinning solution, PMMA (0,399 g) was dissolved in N,N-dimethylformamide (DMF) and then stirred on a magnetic stirrer for about 12 h until a homogeneous solution was obtained. Then, different amounts of complex (**1**), corresponding to 5% (0,0199 g), 10% (0,0399 g), 15% (0,0598 g) and 20% (0,0798 g) by weight, were added to PMMA and mixed for another 12 h at room temperature until a homogeneous solution was obtained.

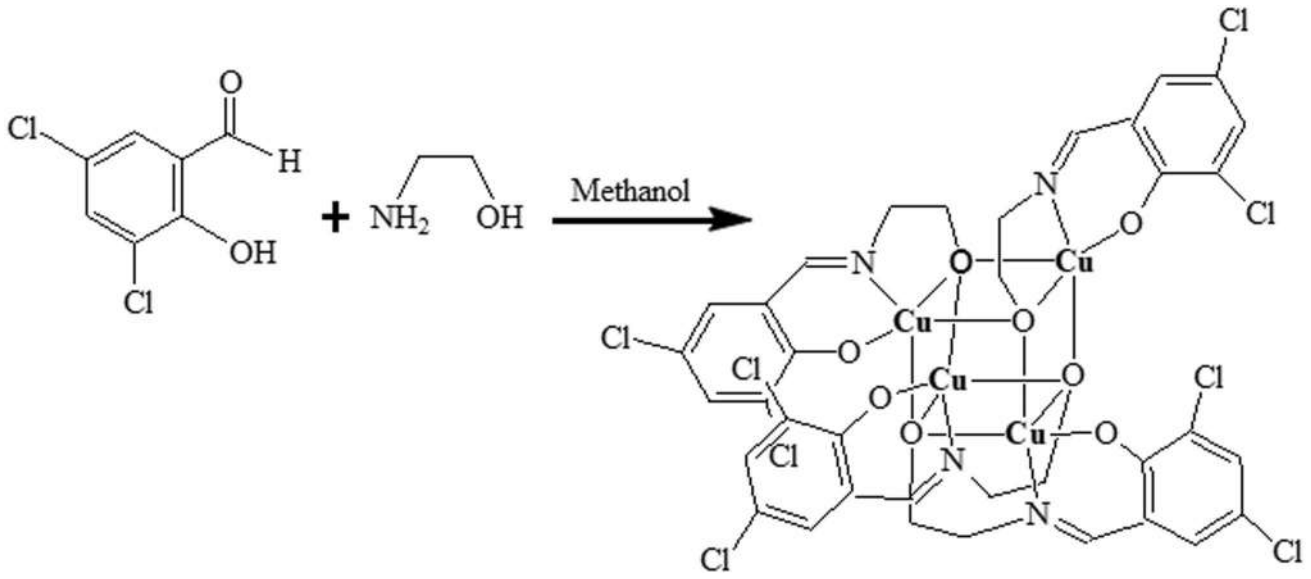

Scheme 1 The synthetic route of complex (**1**)

Electrospinning was carried out in the laboratory spinning unit (SPINGENIX SG-1) under a 13.5 kV by a DC high-voltage generator in horizontal alignment. The final solutions mentioned above were placed in a 5 mL plastic syringe with a capillary with an inside diameter of 0.37 mm. A fluid supply rate was set at 1 mL/h and the distance between the collector and the needle tip was set at 20 cm. Randomly arranged nanofibers were assembled onto an electrically grounded aluminum foil. Next, the composite fibers were placed in a vacuum drying oven at 40 °C for 12 h to remove residual organic solvent. The composite nanofibers obtained in this study were labeled as follows: 5% by weight (A), 10% by weight (B), 15% by weight (C), and 20% by weight (D) for Cu@PMMA.

2.4 X-Ray Crystallography

The single crystal X-ray data for complex (**1**) were collected on an Oxford Diffraction Xcalibur-3 diffractometer equipped with a CCD camera using a monochromatic MoKα source (λ = 0.71073 Å at 296 K). The programs CRYSALIS CCD and CRYSALIS RED [47] were used for the data collection and reductions. The crystal structure was solved using SHELXS [48] by direct methods and refined using SHELXL [49] by using full-matrix least-squares against $|F_{obs}|^2$ with using the interface of the Olex2 program [50]. The detailed supramolecular π-interactions and hydrogen bond geometry were investigated with a Platon 1.17 program [51]. The crystallographic data and structure refinement details for (**1**) have been summarized in Table 1.

Table 1 Crystal data and refinement information for complex (**1**)

Chemical formula	$C_{36}H_{28}Cl_8Cu_4N_4O_8$	
Formula weight (g/mol)	1182.449	
Crystal system	Monoclinic	
Space group	*C2/c*	
Unite cell dimensions	a = 27.661(3) Å	α = 90°
	b = 7.3834(4) Å	β = 130.051(19)°
	c = 27.271(3) Å	γ = 90°
V [Å^3]	4263.4 (14)	
Z	4	
$\rho_{(calc)}$, (g.cm^{-3})	1.842	
μ (mm^{-1})	2.525	
θ_{min}-θ_{max} (°)	3.7–32.5	
h,k,l index	$-40 \le h \le 40$	
	$-11 \le k \le 10$	
	$-40 \le l \le 39$	
Reflections collected	29,038	
Independent reflections	7126 [R_{int}=0.213]	
Goodness-of-fit on F^2	0.76	
R_1 [I > 2σ(I)]	0.060	
wR_2	0.083	

3 Result and Discussion

3.1 Crystal Structure Determination of Complex (1)

X-ray structure analysis shows that the copper atoms of complex (**1**) are five-coordinated and arranged to form a tetranuclear cubane-like structure in the Cu_4O_4 form.

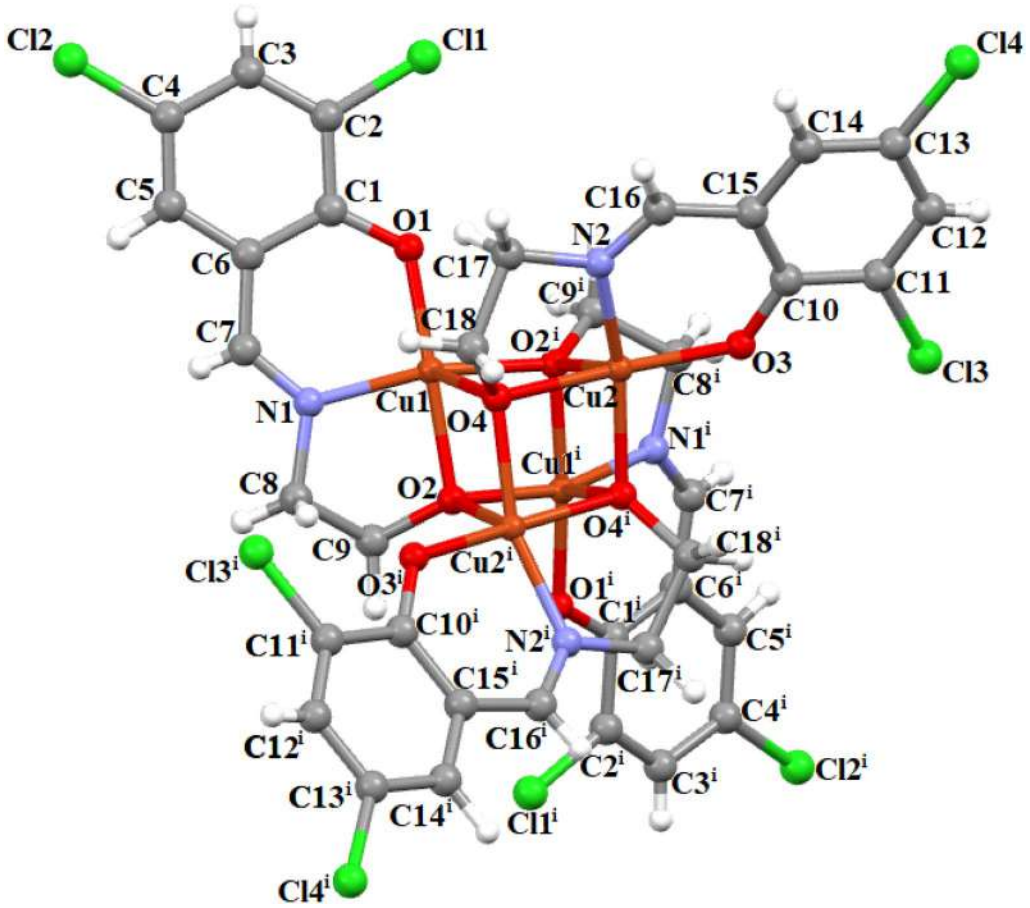

Fig. 1 X-ray crystal structure of complex (**1**)

However, the equatorial position of the five-coordinated Cu(II) atoms is occupied by a phenoxo oxygen atom, an imine nitrogen atom and an alkoxo oxygen atom, while the axial position is occupied by two other alkoxo oxygen atoms of the neighboring Schiff base ligands. X-ray molecular structure of (**1**) with atom labeling is shown in Fig. 1.

The cubane-like core of complex (**1**) and the coordination of copper atoms in the distorted square pyramid structure is shown in Fig. 2. Cu(II) atoms form as a cubane-like structure with the bridging alkoxo oxygens of the Schiff base ligands where the copper ions are located at the diagonal corners of the cube. For the coordination of metal atoms, the coordination deterioration from trigonal pyramidal geometry (TBP) to square bipyramidal (SP) geometry is determined by the Addison distortion index [52, 53]. The distortion index is defined as $\tau = (\alpha - \beta)/60$ where α and β are the largest coordination angles of the metal atom. When the distortion index is $\tau = 0$, the geometry of the complex is square pyramid geometry, and when $\tau = 1$, it is the ideal trigonal bipyramid geometry [52, 53]. The structural deterioration indexes of Cu1 and Cu2 atoms in (**1**) were found as $\tau_{Cu1} = \tau_{Cu1i} = 0.001$ and $\tau_{Cu2} = \tau_{Cu2i} = 0.042$, respectively. In this case, each copper(II) atom has a distorted square pyramidal geometry. The coordination of copper atoms in the distorted square pyramidal geometry and its cubic center in the form of Cu_4O_4 are shown in Fig. 2. Cu1 and Cu2 atoms deviated from the plane formed by the O–N–O atoms of the Schiff base ligand and the oxygen atom in the amine group of the adjacent Schiff base ligand by 0.164 Å and 0.185 Å, respectively. Some selected bond lengths and bond angles between the atoms forming the coordination of the Cu(II) atoms are given in Table 2. The equatorial Cu–O bond lengths range from 1.881 (4) to 1.981 (4) Å, while the axial Cu–O bond lengths are in the range of 2.325 (5)–2.345 (3) Å. This can be explained by the Jahn–Teller extension. The closest intramolecular non-bonding Cu···Cu lengths are 2.892 and 3.242 Å. These values appear to be similar when compared to those in similar copper complexes reported in the literature [54–56].

Figure 3 shows the 3D molecular packing of the cubane-like copper complex. As seen in Fig. 3, complex (**1**) shows a very interesting packaging that is repeated in three dimensions, positioned opposite and parallel to each other. It was found that ligands surrounding the cubic

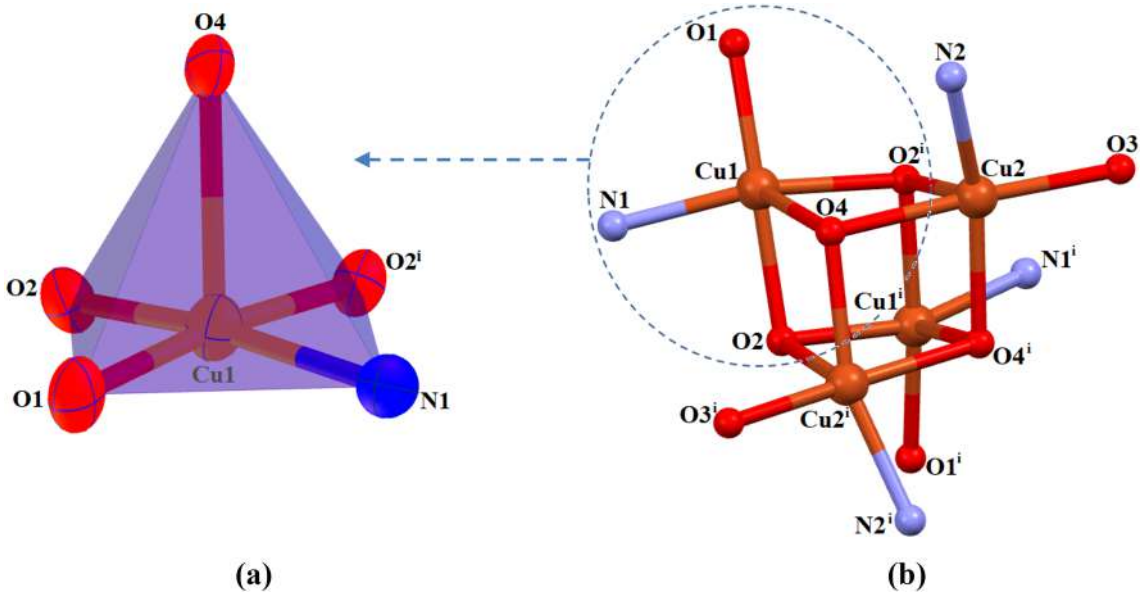

Fig. 2 **a** The coordination environment of Cu(II) ion, **b** Cubane-like core structure of complex (**1**)

Table 2 Some selected bond lengths [Å] and angles [°] for complex (**1**)

Bond lengths (Å)			
Cu1–Cu1^{i}	2.8927 (16)	Cu2–Cu2^{i}	2.9204 (14)
Cu1–O1	1.881 (4)	Cu2–O3	1.883 (3)
Cu1–O2	1.948 (4)	Cu2–O2^{i}	2.324 (5)
Cu1–O2^{i}	1.981 (4)	Cu2–O4	1.962 (3)
Cu1–O4	2.345 (3)	Cu2–O4^{i}	1.969 (3)
Cu1–N1	1.913 (4)	Cu2–N2	1.922 (4)
Bond angles (°)			
O2–Cu1–O1	95.24 (16)	O2–Cu2–O3	104.83 (15)
O2^{i}–Cu1–O1	172.58 (17)	O4^{i}–Cu2–O3	97.18 (16)
O4–Cu1–O1	108.55 (13)	O4–Cu2–O3	173.41 (15)
O4–Cu1–O2^{i}	78.48 (15)	O4^{i}–Cu2–O2	79.24 (14)
O4–Cu1–O2	81.32 (16)	O4–Cu2–O2	81.60 (14)
N1–Cu1–O1	95.18 (18)	N2–Cu2–O3	94.60 (19)
N1–Cu1–O2^{i}	84.70 (18)	N2–Cu2–O2	113.18 (17)
N1–Cu1–O2	163.39 (19)	N2–Cu2–O4	83.98 (18)
N1–Cu1–O4	107.45 (15)	N2–Cu2–O4^{i}	160.02 (15)
Cu2–O2–Cu1^{i}	101.28 (19)	Cu2^{i}–O4–Cu1	100.90 (14)
Cu2–O2–Cu1	98.38 (18)	Cu2–O4–Cu1	97.26 (14)
Symmetry code	$^{i}-x,+y,-z+3/2$		

core in this three-dimensional package structure have weak ligand···ligand interaction with neighboring molecules and the non-bonding Cl···Cl distances are 3.374 Å and 3.491 Å. As can be seen in Fig. 4, the closest intermolecular non-bonding Cu···Cu distance between neighboring molecules along the *bc*-plane is 5.206 Å.

3.2 FT-IR Spectra

The IR spectra of (**1**) and Cu@PMMA nanofibers have been obtained in the region 4000–600 cm^{-1} (Fig. 5). The IR spectra of (**1**) show two absorption bands occurred in the range 2906–2854 cm^{-1} are described to the aliphatic $\nu_{(C-H)}$ stretches [57, 58]. The spectrum shows that the azomethine group $\nu_{(-CH=N-)}$ stretching frequency of the coordinated ligand is observed at 1643 cm^{-1} as compared to 1641 cm^{-1} observed for the free ligand [59]. As expected, the shift of this band towards a higher wavenumber is related to the complexation with the metal ion and free ligand and also indicates M–N linkage which proves the coordination nitrogen atom of the imine group with the metal ion in complex (**1**). The phenolic C–O group of free Schiff base ligand indicates a strong band in the region of 1224–1199 cm^{-1} [60], whereas, in complex (**1**), this band is observed in the lower wavenumber at 1209–1161 cm^{-1}. This band has shifted to a higher wavenumber which is also proving the coordination of the phenolic O atom to the metal center. It is seen that complex (**1**) supports the structure of the examined IR spectrum illuminated by X-ray structure analysis. At the same time, as seen in Fig. 5 the peak at 1727 cm^{-1} could be related to the C=O stretching band of PMMA, the peak mentioned was slightly red-shifted to 1729.84 cm^{-1} in the Cu@PMMA nanofibers, which was attributed to the mutual effect of the oxygen atoms provided by the carbonyl group of PMMA and Cu^{2+} ions in the complex.

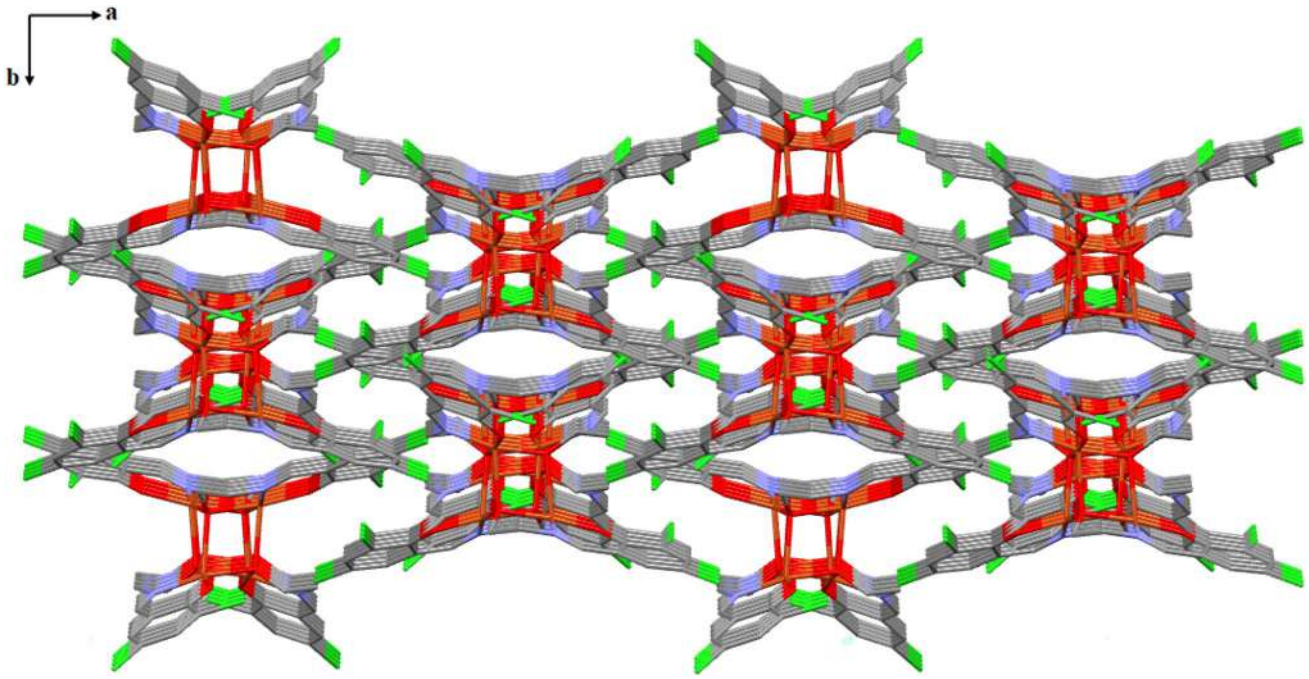

Fig. 3 3D packing structure of (**1**) along the *c*-axis (H atoms omitted for clarity)

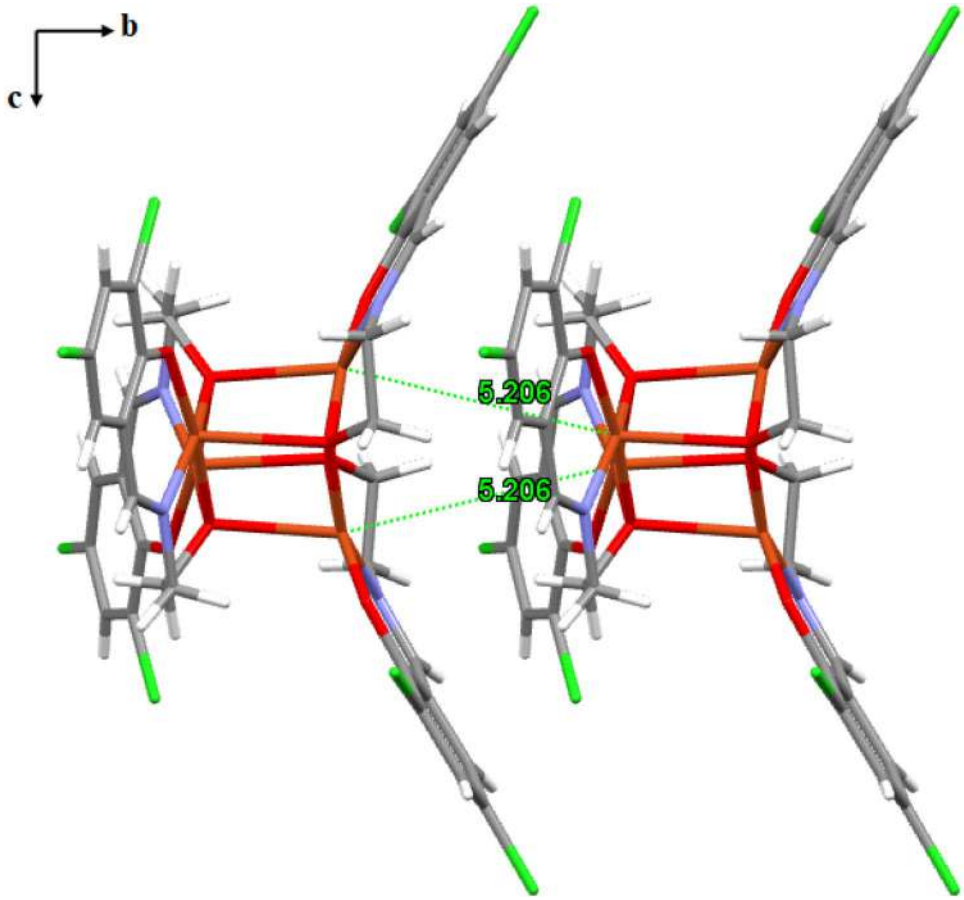

Fig. 4 The distance of intermolecular non-bonding Cu···Cu between the nearest neighboring molecules in the packed structure of (**1**) along the *bc*-plane

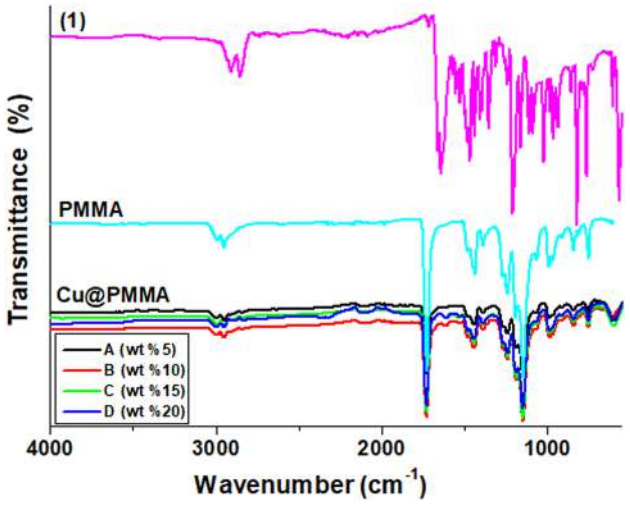

Fig. 5 IR spectra of complex (**1**), PMMA, and Cu@PMMA (5–20wt%) nanofibers

3.3 Morphology of Cu@PMMA Nanofibers

The morphologies of Cu@PMMA composite nanofibers were investigated by using FESEM (5–20 wt%; given as insets in A, B, C and D in Fig. 6). The SEM images show that the fibers are randomly arranged and overlap each other and the surface of the composite nanofibers is smooth without identifiable particles, suggesting that the complex (**1**) might be uniformly dispersed into the nanofibers. The average diameters of Cu@PMMA nanofibers are 148, 196, 270 and 307 nm for A, B, C and D, respectively. Various factors, such as solution concentration, applied voltage, solution velocity, tip-to-collector distance, and solution properties (such as polarity, surface tension and electric conductivity), have a well-known influence on the diameters and morphology of electrospun nanofibers [61]. Among these factors, polymer concentration is a critical determinant of the viscosity of the polymer solution, which significantly affects the electrospinning process. Therefore, increasing percentages of complex (**1**) added to PMMA/DMF solutions increased the viscosity of the solutions, resulting with increasing nanofiber diameters.

3.4 Photoluminescence Properties

The solid-state emission properties of PMMA, complex (**1**), and Cu@PMMA composite fibers were recorded at room temperature under UV excitation at 349 nm (Fig. 7). The PMMA fibers give a broad emission band centered at 522 nm due to the $\pi \rightarrow \pi^*$ transition of PMMA under UV excitation at 349 nm [62, 63]. The photoluminescence properties of Cu@PMMA fibers were studied in detail depending on the additives of 5, 10, 15 and 20% by weight of complex (**1**). It is important to research the difference between the solid-state photoluminescence spectra of complex (**1**) and Cu@PMMA composite fibers. The PL spectra of the complex (**1**) and the Cu@PMMA composite nanofibers showed strong and characteristic emission bands. The emission spectrum of complex (**1**) shows a broad band with a maximum wavelength of 470 nm. The emission properties created by this broadband probably appear as ligand-centered charge transfer. The blue emission band formed by complex (**1**) with a central wavelength of 470 nm can be defined as the $n \rightarrow \pi^*$ or $\pi \rightarrow \pi^*$ ligand-centered transition [60, 64].

When the photoluminescence intensities of complex (**1**) and Cu@PMMA composite fibers are compared, no difference was observed in the shape and position of the characteristic peaks when the doping concentration of complex (**1**) increased. However, the luminescence intensity increased with the complex (**1**) concentration and the maximum emission intensity was 15% by weight in the composition. Following this, the luminescence intensities gradually decrease with a further increase of Cu^{2+} concentration, which so-called concentration quenching phenomenon [65, 66].

Concerning the mechanism of energy transfer in composite fibers, the concentration quenching phenomenon of photoluminescence is attributed to the non-radiative energy transfer among the same luminescence centers, such as Cu^{2+} ions here. The critical distance (Rc), among activator ions at the regime of concentration quenching, is discussed for investigating the energy transfer mechanism. The critical transfer distance (R_c) and critical concentration value (x_c) can be calculated using the relation given by Blasse

$$R_c \approx 2\left(\frac{3V}{4\pi x_c N}\right)^{1/3}$$

where V is the unit cell volume and N is the number of lattice sites in the unit cell available for activator ions [67]. For Cu@PMMA nanofibers, V = 1182.449 Å^3, N = 4, and also x_c is equal to the critical concentration of 0.15. Thus, the R_c is calculated to be 9.80 Å. Non-radiative energy transfer can result from two main mechanisms: multipolar interaction and exchange interaction. However, the calculated optimum R_c value implies a low probability of the exchange interaction mechanism. The critical distance of the exchange interaction is responsible for the energy transfer of the forbidden transition. According to available literature, the typical critical distance is about 5 Å [68–70]. Based on the above calculations, the mechanism of exchange interaction does not play an important role in the energy transfer process between Cu^{2+} ions in the host matrix. Thereby, we estimate that multipolar-multipolar interaction is responsible for the predominant concentration quenching of Cu^{2+} ions in Cu@

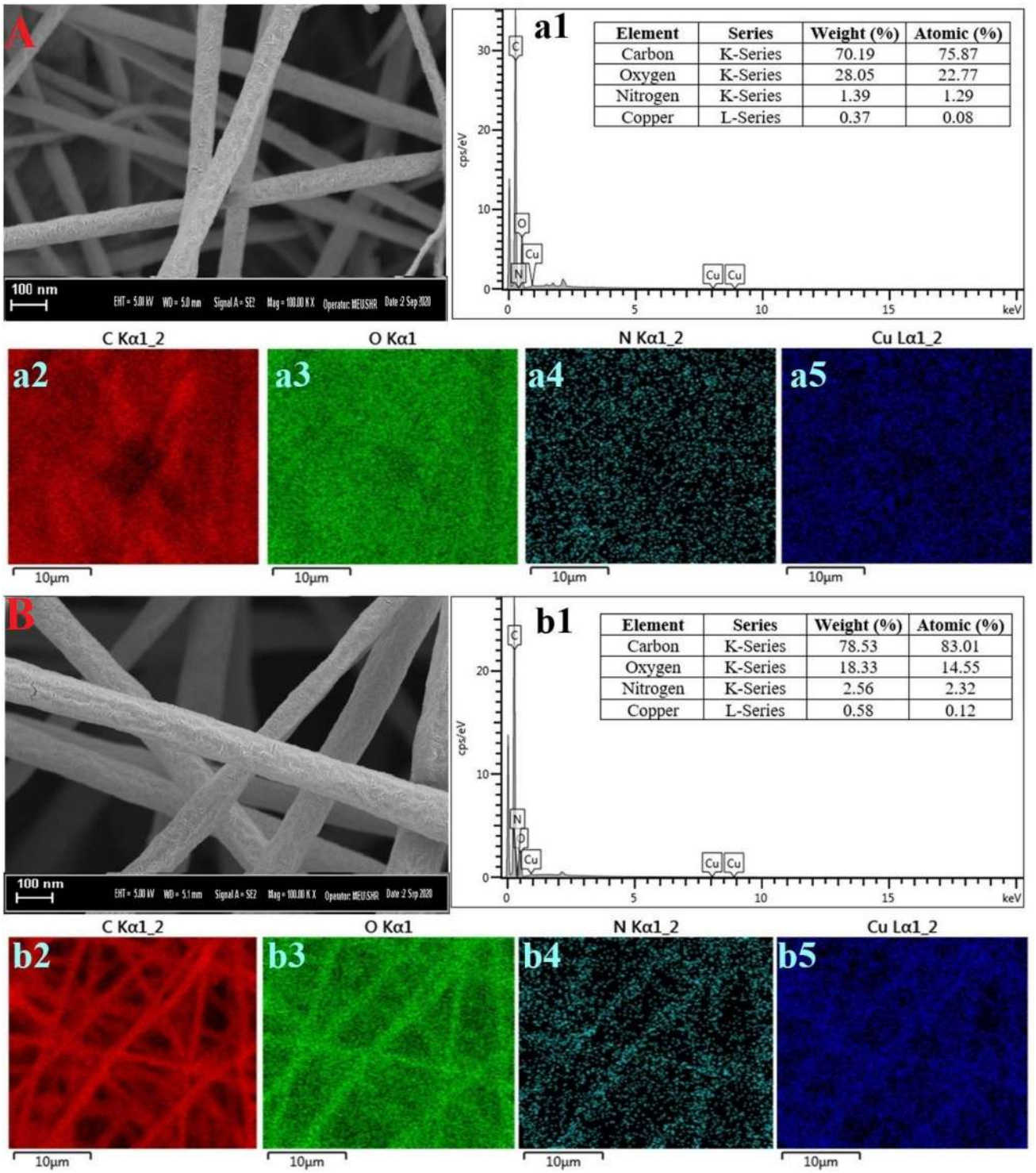

Fig. 6 FESEM images and size distribution and EDX (**a1**–**d1**) of Cu@PMMA nanofibers (5–20 wt%; given as insets in A, B, C and D) and elemental mapping of the carbon (**a2**–**d2**), oxygen (**a3**–**d3**), nitrogen (**a4**–**d4**) and copper (**a5**–**d5**)

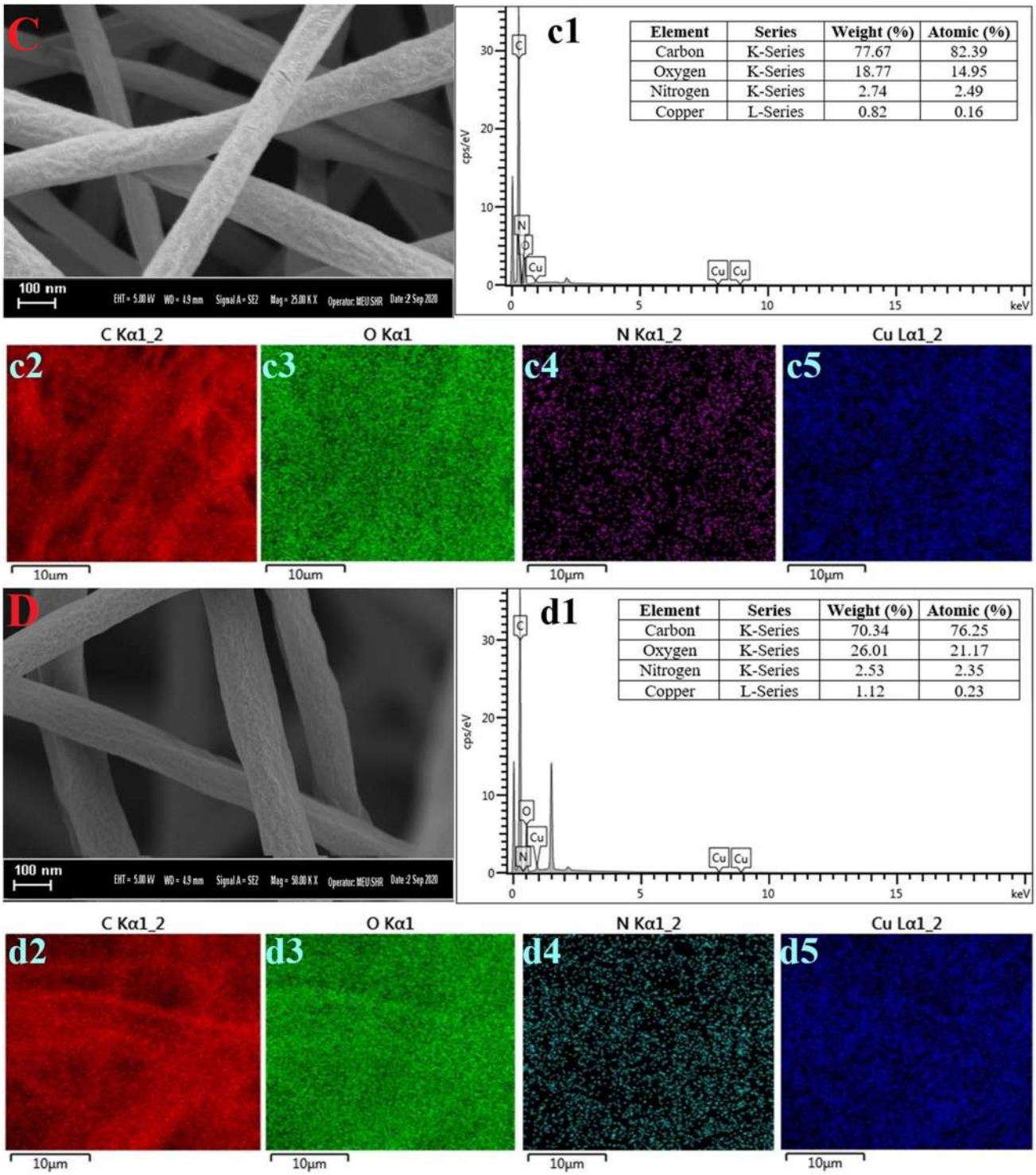

Fig. 6 (continued)

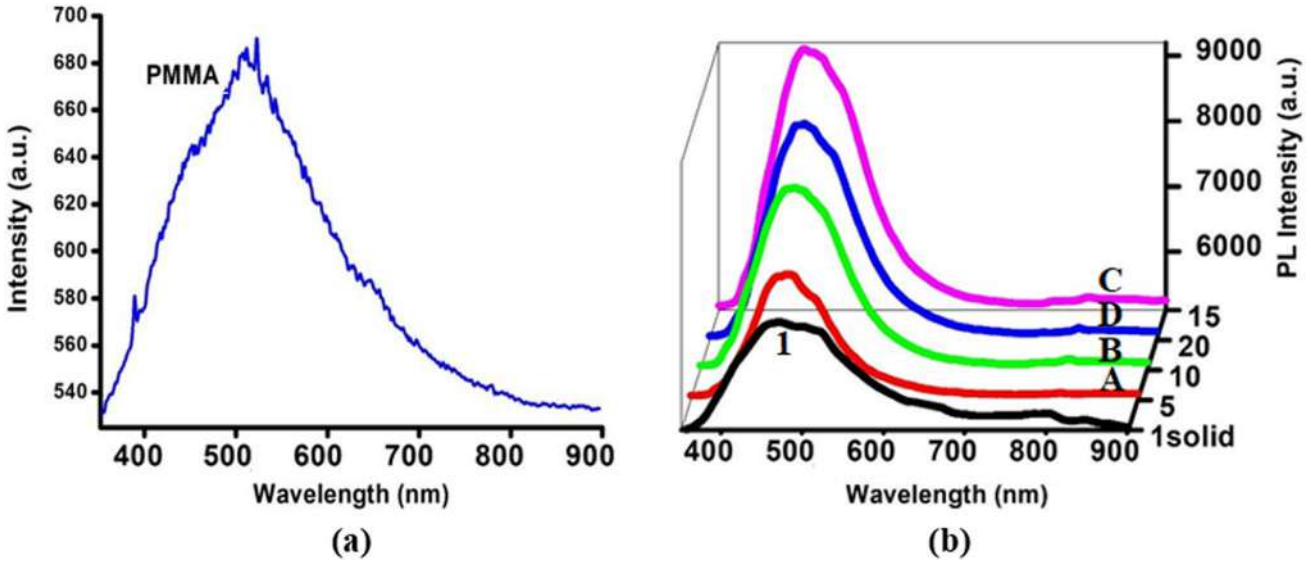

Fig. 7 The solid-state emission spectra of, **a** PMMA, **b** Complex (**1**) and Cu@PMMA (5–20 wt%) nanofibers at room temperature (λ_{exc} = 349 nm)

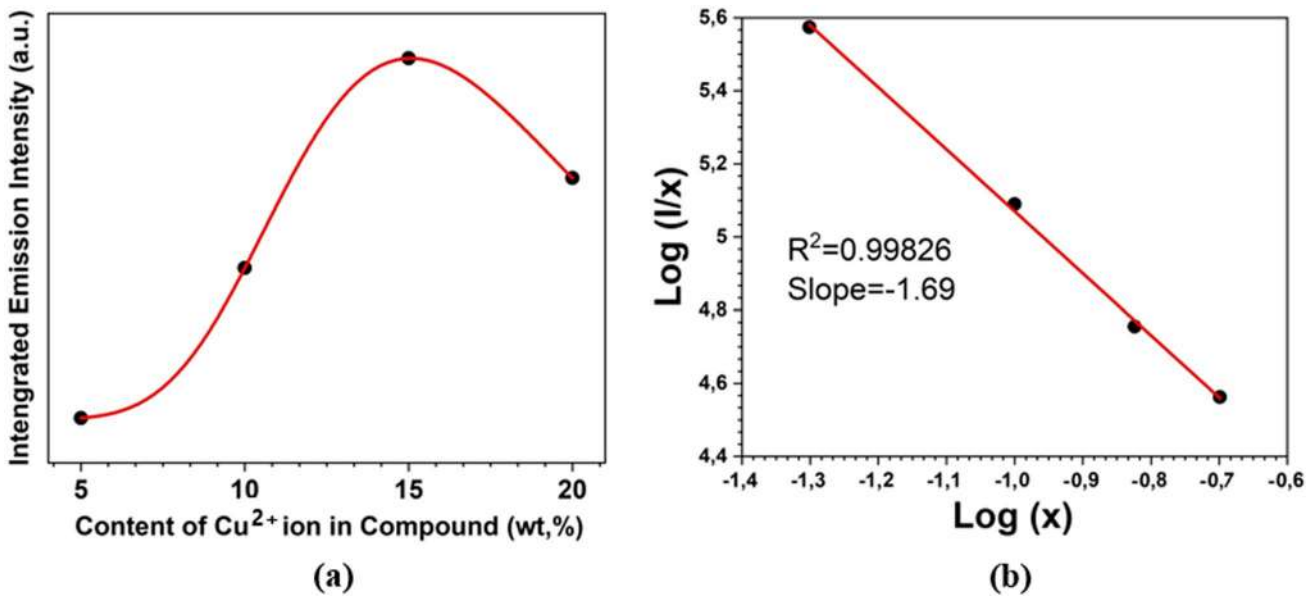

Fig. 8 **a** Comparison of the total emission intensities of Cu@PMMA (5–20 wt%) nanofibers at room temperature due to complex (**1**) contribution (λ_{exc} = 349 nm), **b** Fitting of Log (I/x) against Log(x) in Cu@PMMA, x = Cu(II) (x = 0.05, 0.1, 0.15 and 0.2)

PMMA. Based on Van Uitert and Dexter-Schulman's view, the emission intensity (I) per activator ion is related as below [71, 72];

$$lg\left(\frac{I}{x}\right) \approx -\frac{\theta}{3}lg(x) + K'$$

where x represents the concentration of the activator ion, and K′ is a constant for the same excitation condition for a given host matrix. The value of the fitting constant θ are 3, 6, 8 and 10 and for this increasing order are the exchange interaction, dipole-dipole, dipole-quadruple and quadruple-quadruple interactions, respectively. The linear fitting has

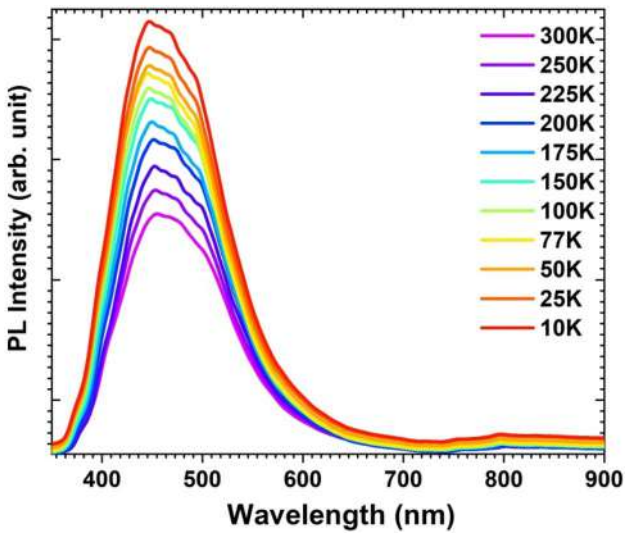

Fig. 9 PL spectra of Cu@PMMA (15%) composite nanofiber sample from 10 to 300 K

been performed on the dependence lg(I/x) on lg(x) and the slope of the solid red line calculated is − 1.69 in Fig. 8b. As a result, the value of θ can be calculated as 5.07, which is close to 6. As a result of dipole-dipole interaction, quenching concentration occurs in Cu@PMMA nanofibers [66, 73–75].

The other effective approximation for the luminescence concentration quenching (CQ) effect can be summarized as follow:

It could be considered that the distribution in the complex PMMA host is close to homogeneous at low percentages. Thus, fading of luminescence due to metal-metal interactions is prevented. However, it can be seen that the emissions of the Cu@PMMA matrix were remarkably enhanced with the increasing amount of Cu^{2+} and reached its maximum value at 15 wt%. When the further increase doping amount of the Cu^{2+} ions in the complex, the PMMA matrix cannot avoid metal-metal interactions. Subsequently, the luminescence intensity starts to decrease due to the concentration quenching effect occasioned by the increase in doped Cu^{2+} ions in Cu@PMMA [76].

In Fig. 8a, it has been determined that the photoluminescence emission intensity increased as the weight% of complex (**1**) (up to 15%) increased in composite nanofiber materials. With the increase of the percentage of complex (**1**) in the composite nanofiber material, due to the clustering of Cu^{2+} centers at such a microscopic level, the increasing complex (**1**) content after this level started to reduce the intensity of diffusion. Such a reduction indicates that complex (**1**) forms an inhomogeneous distribution in the polymer matrix and aggregates at the molecular level [77–80].

Thermal evaluation is crucial for a better understanding of optical properties. Low-temperature measurements reveal some spectral profiles. The resolvable spectral peaks can be analyzed as detailed in cryogenic temperatures. On the contrary, some spectral detail can be disappearing at room temperature due to thermal expansion [81].

Temperature-dependent PL measurements of the Cu@PMMA (15 wt%) composite nanofiber sample were carried out within the temperature range 10–300 K and shown in Fig. 9. From the figure, it can be seen that the peak shapes do not get influenced due to the temperature variation and the main emission band is slightly red-shifted with increasing temperature. We estimate that this may be due to the following reasons. With the temperature increased, the crystal field strength decreases due to the lattice thermal broadening and the band gap narrows with the interaction of electrons and lattices [81, 82].

The emission intensities of Cu@PMMA (15 wt%) composite fiber sample decreased obviously with temperature from 10 to 300 K, which should be caused by thermal quenching. The enhancement of temperature causes the reduction in the intensity of the peak since the temperature enhancement the number of molecules in the excited state more and more increases, while the ratio of the number of molecules in the excited state of the low energy level is reduced. Meanwhile, the emission intensity band undergoes a remarkable decrease due to the increase in the thermally activated non-radiative transitions [83].

The International commission on illumination (CIE) chromaticity coordinates for both complex (**1**) and Cu@PMMA composite fiber samples have been computed based on the corresponding PL spectra and shown in Fig. 10. When compared with the CIE coordinates of complex (**1**), it can be noticed that the colour coordinates moving towards the blue region with the addition of Cu(II) complex into the electrospun Cu@PMMA nanofibers. The CIE plots indicate that the color coordinates of complex (**1**) are located at (0.292, 0.305) and it is shifted to (0.269, 0.272) with Cu@PMMA (15 wt%) nanofiber obtained by implementation of the electrospinning process. For Cu@PMMA (15 wt%), the color coordinates shifted to blue with decreasing the temperature [84].

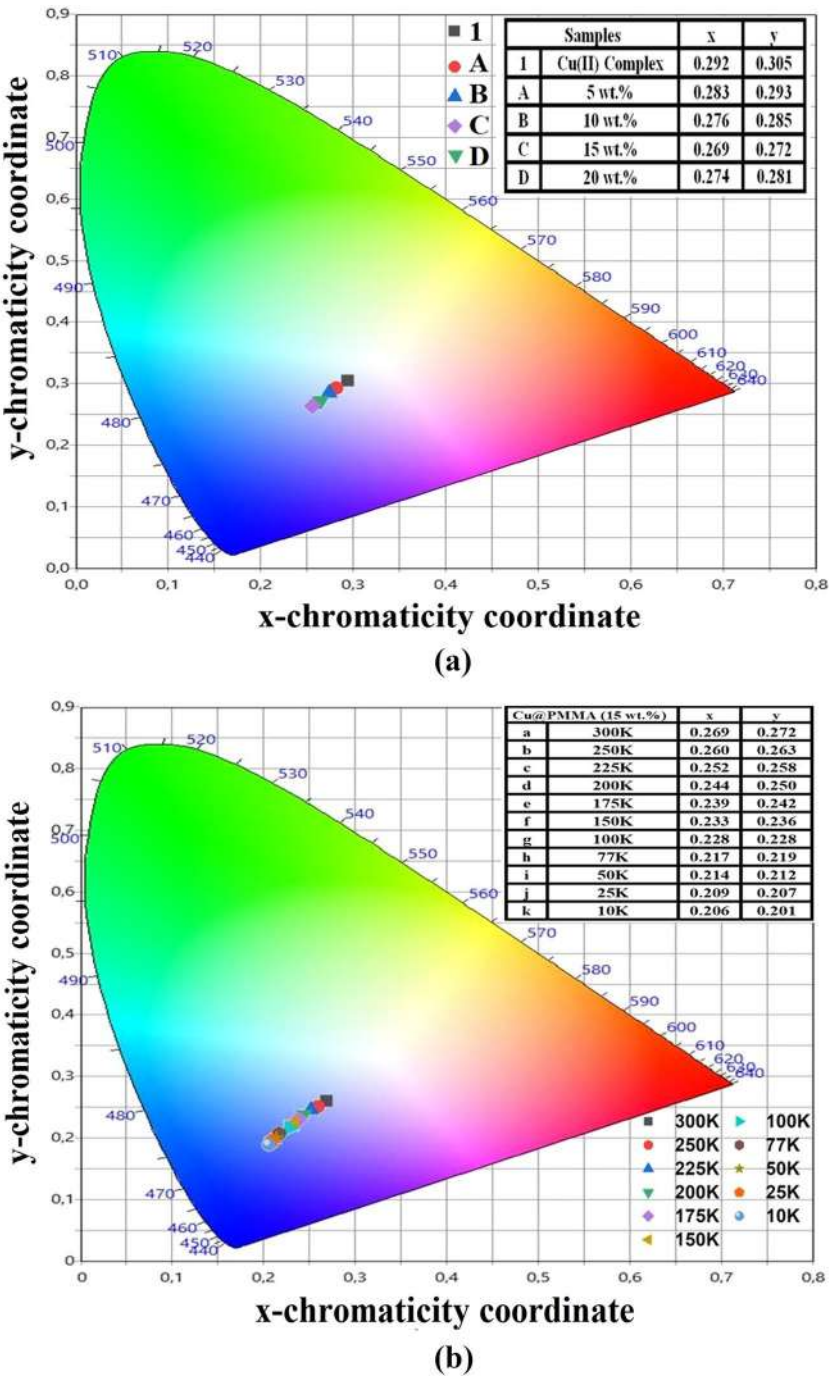

Fig. 10 Color coordinates in the CIE-1931 chromaticity diagrams, **a** for complex (**1**) and Cu@PMMA nanofibers (given as insets in A, B, C and D), **b** for Cu@PMMA (15%) composite nanofiber sample in the temperature range 10–300 K

4 Conclusion

In this study, tetranuclear copper(II) Schiff base complex (**1**) was synthesized and its crystal structure was investigated by single crystal X-ray diffraction technique. Cu@PMMA composite nanofibers were prepared successfully by using the electrospinning technique with different concentrations (5–20 wt%) of complex (**1**). The morphological properties and solid-state photoluminescence properties of Cu@PMMA nanofibers at room temperature and low temperature was investigated. The well-aligned photoluminescent nanofibers have average diameters from 148 to 307 nm.

The experimental findings demonstrated a pronounced enhancement in the room temperature photoluminescence (PL) emissions of Cu@PMMA nanofibers as the Cu^{2+} content increased. This increase continued until it reached a peak at 15 wt%. Subsequently, a phenomenon known as concentration quenching occurred due to the escalating concentration of Cu^{2+} ions. This led to undesired

metal-metal interactions, resulting in a decrease in the luminescence intensity. Notably, the PMMA matrix exhibited limited capability to mitigate these interactions, further contributing to the observed decline in luminescence intensity. Temperature-dependent photoluminescence (PL) measurements were conducted on the Cu@PMMA (15 wt%) nanofiber sample over a temperature range of 10 to 300 K. A notable observation was made as the temperature increased: the emission intensities of the Cu@PMMA nanofibers exhibited a clear decline from 10 to 300 K. This decrease in emission intensity can be attributed to thermal quenching effects induced by the elevated temperatures. The Cu@PMMA composite nanofibers exhibited blue emission with 349 nm UV excitation. Brilliant values of the chromaticity coordinates of the prepared photoluminescent nanofibers predict their possible use in blue solid-state lighting applications.

Supplementary Information The online version contains supplementary material available at https://doi.org/10.1007/s10904-023-02807-5.

Author Contributions YA: Project administration, Writing–original draft, Writing–review and editing, Formal Analysis. EG: Conceptualization, Methodology. MBC: Visualization and Methodology, Data curation. FK: Methodology, Data curation. HKS: Visualization and Software.

Funding The authors thank to the Research Funds of Balikesir University (Grant No. BAP-2019/083) for the financial support and Balikesir University, Science and Technology Application and Research Center (BUBTAM) for the use of the Photoluminescence Spectrometer.

Declarations

Competing interests The authors declare that they have no known competing financial interests or personal relationships that could have appeared to influence the work reported in this paper.

References

1. J. Bai, Y. Liu, Y. Hou, S. Wang, Mater. Chem. Phys. **217**, 486 (2018)
2. E. Zussman, A. Greiner, J.H. Wendorff, A.L. Yarin, Z. Sun, Adv. Mater. **15**, 1929 (2003)
3. Z.M. Huang, Y.Z. Zhang, M. Kotaki, S. Ramakrishna, Compos. Sci. Technol. **63**, 2223 (2003)
4. Y. Xin, Z.H. Huang, E.Y. Yan, W. Zhang, Q. Zhao, Appl. Phys. Lett. **89**, 053101 (2006)
5. M. Mondragón, E. Arias, L.E. Elizalde, M.E. Castañeda, I. Moggio, J. Lumin. **192**, 745 (2017)
6. H. Wang, Y. Li, C. Zhang, Q. Yang, S. Wang, Y. Li, L. Sun, J. Alloys Compd. **488**, 414 (2009)
7. N.C. Deıtzel, J.M. Kleinmeyer, J. Haris, B. Tan, Polymer **42**, 261 (2001)
8. S. Qin, X. Wang, J. Appl. Polym. Sci. **102**, 1285 (2006)
9. S. Lin, Q. Cai, J. Ji, G. Sui, Y. Yu, X. Yang, Q. Ma, Y. Wei, X. Deng, Compos. Sci. Technol. **68**, 3322 (2008)
10. J.-P. Chen, Y.-S. Chang, Colloids Surf. B **86**, 169 (2011)
11. H. Jayakumar, R. Prabaharan, M. Nair, S.V. Tamura, Biotechnol. Adv. **28**, 142 (2010)
12. R. Sahay, P.S. Kumar, R. Sridhar, J. Sundaramurthy, J. Venugopal, S.G. Mhaisalkar, S. Ramakrishna, J. Mater. Chem. **22**, 12953 (2012)
13. R. Vasita, D.S. Katti, Int. J. Nanomed. **1**, 15 (2006)
14. T.-T. Phan, P. See, S.-T. Lee, S.-Y. Chan, J. Trauma **51**, 927 (2001)
15. J.A. Matthews, G.E. Wnek, D.G. Simpson, G.L. Bowlin, Biomacromolecules **3**, 232 (2002)
16. G.A. Shawki, M.M. Hereba, A.M. Romanian, J. Biophys. **20**, 335 (2010)
17. I. Alghoraibi, S. Alomari, *Handbook of Nanofibers* (Springer International Publishing, Cham, 2018), pp.1–46
18. D. Li, Y. Xia, Adv. Mater. **16**, 1151 (2004)
19. X. Zhang, S. Wen, S. Hu, L. Zhang, L. Liu, J. Rare Earths **28**, 333 (2010)
20. A. Camposeo, F. Di Benedetto, R. Cingolani, D. Pisignano, Appl. Phys. Lett. **94**, 043109 (2009)
21. W.-E. Teo, S. Ramakrishna, Compos. Sci. Technol. **69**, 1804 (2009)
22. D.-G. Yu, L.-M. Zhu, K. White, C. Branford-White, Health **01**, 67 (2009)
23. S. Kidoaki, I.K. Kwon, T. Matsuda, Biomaterials **26**, 37 (2005)
24. M. Asadi, S. Shahabuddin, A. Mollahosseini, J. Kaur, R. Saidur, J. Inorg. Organomet. Polym. Mater. **29**, 1057 (2019)
25. R.H. Berg, *Holm, Iron-Sulfur Proteins* (Wiley-Interscience, New York, 1982)
26. R.H. Holm, S. Ciurli, J.A. Weigel, Prog. Inorg. Chem. **39**, 1–74 (1990)
27. M.A. Halcrow, J.C. Huffman, G. Christou, Angew. Chem. Int. Ed. Engl. **34**, 889 (1995)
28. M.A. Halcrow, J.-S. Sun, J.C. Huffman, G. Christou, Inorg. Chem. **34**, 4167 (1995)
29. K. Mai, H.J. Köcker, R.M. Wocadlo, S. Massa, W. Dehnicke, Angew. Chem. Int. Ed. Engl. **34**, 1235 (1995)
30. L. Merz, W. Haase, J. Chem. Soc. Dalton Trans. **11**, 1594 (1978)
31. L. Schwabe, W. Haase, J. Chem. Soc. Dalton Trans. 1909 (1985)
32. J.W. Hall, W.E. Estes, E.D. Estes, R.P. Scaringe, W.E. Hatfield, Inorg. Chem. **16**, 1572 (1977)
33. J. Sletten, A. Soerensen, M. Julve, Y. Journaux, Inorg. Chem. **29**, 5054 (1990)
34. A.P. Ginsberg, J.A. Bertrand, R.I. Kaplan, C.E. Kirkwood, R.L. Martin, R.C. Sherwood, Inorg. Chem. **10**, 240 (1971)
35. K. Hussain Reddy, P. Sambasiva Reddy, P. Ravindra Babu, Transit. Met. Chem. **25**, 505 (2000)
36. S. Kumar, G. Jain, B.P. Singh, S.R. Dhakate, J. Nanomater. **2020**, 1 (2020)
37. S. Kumar, G. Jain, K. Kumar, A. Gupta, J.S. Tawale, B.P. Singh, S.R. Dhakate, P.D. Sahare, J. Nanomater. **2022**, 1 (2022)
38. S. Kumar, G. Jain, K. Kumar, A. Gupta, B.P. Singh, S.R. Dhakate, RSC Adv. **10**, 24855 (2020)
39. G. Sanjeev Kumar, K. Jain, B.P. Kumar, Singh, S.R. Dhakate, Polym. Sci. Ser. A **64**, 367 (2022)
40. S. Kumar, G. Jain, K. Kumar, A. Gupta, B.P. Singh, S.R. Dhakate, Appl. Nanosci. **10**, 3857 (2020)
41. J.A.G. Hamilton, A. Ozarowski, E. Archibong, S. Thomas, W. Serrano-Garcia, S.A. Stoian, C. Weider, N. Mateeva, Mater. Lett. **238**, 58 (2019)
42. M. Arvand, M.S. Ardaki, Anal. Chim. Acta **986**, 25 (2017)
43. S. Tang, C. Shao, Y. Liu, S. Li, R. Mu, J. Phys. Chem. Solids **68**, 2337 (2007)
44. G.N.S. Vijayakumar, S. Devashankar, M. Rathnakumari, P. Sureshkumar, J. Alloys Compd. **507**, 225 (2010)
45. M. Hashmi, S. Ullah, I.S. Kim, Curr. Res. Biotechnol. **1**, 1 (2019)

46. H. Xiang, Y. Long, X. Yu, X. Zhang, N. Zhao, J. Xu, CrystEngComm **13**, 4856 (2011)
47. CrysAlis^{Pro} Software, Version 1.171.41.93a, Rigaku Corporation, Oxford, UK (2020)
48. G.M. Sheldrick, Acta Crystallogr. **A64**, 112 (2008)
49. G.M. Sheldrick, Acta Crystallogr. C **71**, 3 (2015)
50. O.V. Dolomanov, L.J. Bourhis, R.J. Gildea, J.A.K. Howard, H. Puschmann, J. Appl. Crystallogr. **42**, 339 (2009)
51. A.L. Spek, Acta Crystallogr. D **65**, 148 (2009)
52. J.A. Hathaway, B.J. Wilkinson, G. Gillard, R.D. McCleverty (eds.), *Comprehensive Coordination Chemistry II* (Pergamon Press, Oxford, UK, 1987)
53. A.W. Addison, T.N. Rao, J. Reedijk, J. van Rijn, G.C. Verschoor, J. Chem. Soc. Dalton Trans. **7**, 1349 (1984)
54. J.-F. Dong, L.-Z. Li, T. Xu, H. Cui, D.-Q. Wang, Acta Crystallogr. E **63**, m1501 (2007)
55. S.-F. Si, J.-K. Tang, D.-Z. Liao, Z.-H. Jiang, S.-P. Yan, Inorg. Chem. Commun. **5**, 76 (2002)
56. M. Dey, C.P. Rao, P.K. Saarenketo, K. Rissanen, Inorg. Chem. Commun. **5**, 380 (2002)
57. Y. Yahsi, E. Gungor, M.B. Coban, H. Kara, Mol. Cryst. Liq. Cryst. **637**, 67 (2016)
58. C. Kocak, G. Oylumluoglu, A. Donmez, M.B. Coban, U. Erkarslan, M. Aygun, H. Kara, Acta Crystallogr. C **73**, 414 (2017)
59. M. Nandy, D. Saha, C. Rizzoli, S. Shit, Z. Naturforsch. B **72**, 1 (2017)
60. Y. Acar, H. Kara, E. Gungor, M.B. Coban, Mol. Cryst. Liq. Cryst. **664**, 165 (2018)
61. X. Li, G. Shen, X. Jin, M. Liu, L. Shi, J. Lu, J. Mater. Sci. **51**, 2072 (2016)
62. H. Kara, G. Oylumluoglu, M.B. Coban, J. Clust. Sci. **31**, 701 (2020)
63. M.B. Coban, E. Gungor, Y. Acar, F. Kuru Alpaslan, H. Kara Subasat, CrystEngComm **22**, 6116 (2020)
64. H. Choopani Jouybari, R. Alizadeh, H. Banisaeed, V. Amani, Inorg. Chim. Acta **506**, 119553 (2020)
65. J. Chen, Y. Song, Y. Sheng, M. Chang, X. Xie, M.M.A. Abualrejal, H. Guan, Z. Shi, H. Zou, J. Alloys Compd. **716**, 144 (2017)
66. M. Jin, N. Li, H. Shao, D. Li, F. Sun, W. Yu, X. Dong, Ceram. Int. **48**, 31548 (2022)
67. G. Blasse, Phys. Lett. A **28**, 444 (1968)
68. J. Hakami, Ã.H. Kaynar, M. Ayvacikli, M.B. Coban, J. Garcia-guinea, P.D. Townsend, M. Oglakci, N. Can, Ceram. Int. **48**, 32256 (2022)
69. S.U. Bhonsule, D. Marghade, S.P. Wankhede, Mater. Today Proc. **15**, 626 (2019)
70. Z. Wang, Z. Wang, J. Liu, Y. Li, X. Meng, K. Qiu, Q. Bao, Y. Chen, Z. Yang, P. Li, J. Lumin. **207**, 602 (2019)
71. L.G. Van Uitert, J. Electrochem. Soc. **114**, 1048 (1967)
72. D.L. Dexter, J.H. Schulman, J. Chem. Phys. **22**, 1063 (1954)
73. G. Souadi, U.H. Kaynar, M. Ayvacikli, M.B. Coban, M. Oglakci, A. Canimoglu, N. Can, Appl. Radiat. Isot. **175**, 109820 (2021)
74. P.D. Bhoyar, R. Choithrani, S.J. Dhoble, Solid State Sci. **57**, 24 (2016)
75. Ł Marek, M. Sobczyk, J. Non Cryst. Solids. **576**, 121238 (2022)
76. S. Rodríguez, P. Elizondo, S. Bernès, N. Pérez, R. Bustos, E. García-España, Polyhedron **85**, 10 (2015)
77. Z. Kotan, M. Ayvacikli, Y. Karabulut, J. Garcia-Guinea, L. Tormo, A. Canimoglu, T. Karali, N. Can, J. Alloys Compd. **581**, 101 (2013)
78. U.H. Kaynar, S.C. Kaynar, M. Ayvacikli, Y. Karabulut, G.O. Souadi, N. Can, Radiat. Phys. Chem. **168**, 108617 (2020)
79. S.H. Nannuri, A.R. Samal, C.K. Subash, C. Santhosh, S.D. George, J. Alloys Compd. **777**, 894 (2019)
80. X. Xue, M. Thitsa, T. Cheng, W. Gao, D. Deng, T. Suzuki, Y. Ohishi, Opt. Express **24**, 26307 (2016)
81. A. Mondal, J. Manam, Ceram. Int. **46**, 23972 (2020)
82. J. Wu, Z. Xu, J. Chen, L. He, Infrared Phys. Technol. **92**, 18 (2018)
83. R. Gopal, A. Kumar, J. Manam, Mater. Chem. Phys. **272**, 124960 (2021)
84. L. Aziz, N. Sabih, S. Mehmood, A. Ali, M.U. Hassan, A.S. Bhatti, Ceram. Int. **46**, 9794 (2020)